

Elastoplastic Damage Model for Concrete under Triaxial Compression and Reversed Cyclic Loading

J. Zhang,¹ L. Ma,² and Z. X. Zhang³

School of Civil Engineering and Mechanics, Huazhong University of Science and Technology, Wuhan, China

¹ zhang_ji@hust.edu.cn

² mal1994@hust.edu.cn

³ zzx027027@163.com

The elastoplastic damage model for concrete is elaborated that can be applied to various stress states. In the previous study (2016) the 3D elastoplastic damage model, based on the Lubliner yield criterion and Drucker–Prager flow rule, was constructed. The simplified forms of the two functions set certain limitations on the calculations in true triaxial compression and high confining pressure. Improved accuracy of yield surface and potential plastic surface is required. The Menétrey–Willam yield criterion is adopted and analyzed in the effective stress space. The methods that define the hardening and softening functions through the volume plastic strain are no longer used in some successful 3D models since they employ double hardening and two-scalar damage to describe an increase in effective yield stress and degradation of stiffness. The suppression of damage evolution in triaxial compression is taken into account through the confining net decomposition of stress. The validation of specific parameters in the potential plastic function of the novel model is verified. The iteration return mapping algorithm is worked out and implemented. The reliability of the proposed model is corroborated by numerical simulation results compared with existing experimental data.

Keywords: elastoplastic damage, effective stress, hardening law, confining net decomposition, return mapping algorithm.

Introduction. Concrete materials exhibit complex nonlinear characteristics, such as unilateral effects, stiffness degradation, post-peak strength softening, a significant increase in strength and ductility under confining pressure, tension–compression softening and irrecoverable deformation because of various failure mechanisms including microcrack (microdefect) expansion and friction. Damage is caused by the initiation and propagation of microcracks. Plasticity is mainly due to frictional sliding along closed microcracks under compression. Under triaxial compression, with the increase of confining pressure, there is a gradual transition from quasi-brittle to ductile behavior for concrete, which should be paid particular attention to.

Elasticity, plasticity, and damage mechanics, etc. have been widely applied to establish concrete constitutive models. Since pure plasticity models fail to describe stiffness degradation and unilateral effects and are not appropriate for cyclic loading and reversed loading [1–4] while pure damage models fail to reflect irrecoverable deformation, plasticity and damage should be used simultaneously to simulate the nonlinear behavior of concrete. Elastoplastic damage models, which combine plasticity and damage, have drawn considerable attention in current researches [5–15] and become a kind of mainstream constitutive theory which can adequately reflect the mechanical properties of concrete. Some models have only one hardening variable and one damage variable and cannot reflect the independent hardening and damage in tension and compression [8, 9]. Some models utilize damage mechanics for stress and plasticity for compression but fail to realize the two aspects at the same time [6, 11]. Some models, such as those proposed by Abu Al-Rub and Kim [5] and Omidi and Lotfi [10], are not applicable to triaxial compression.

There are two approaches to introduce the plastic strain and its evolution law into the modeling process of damage constitutive relation. One relies on the Cauchy stress space where the evolution equation of plastic strain is formulated [1–4]. Cauchy stress characterizes the nominal stress at the macroscopic level. The macroscopic stress will decrease after the material enters the softening stage. An elastoplastic damage model based on the Cauchy stress space will inevitably involve the problem of contraction of the yield surface. Consequently, there will be a series of problems of numerical convergence and stability. Another alternative is based on the effective stress space [8, 10, 13, 15], where the yield surface is always in the process of expansion without contraction during loading, so the troublesome problem mentioned above can be avoided.

In the previous work by Zhang et al. [15], an elastoplastic damage model, which employed the Lubliner yield criterion and Drucker–Prager flow rule, was developed. The characteristics of concrete, such as unilateral effects, stiffness degradation, post-peak strength softening, increasing strength and ductility under confining pressure, irrecoverable deformation, etc., were reflected successfully. But owing to the simple forms of the yield function and plastic potential function, which lead to straight meridians of the yield surface and plastic potential surface, the calculations in true triaxial compression and high confining pressure are limited. Consequently, more accurate yield function and plastic potential function are required, which are to be studied in the present work.

The yield criterion proposed by Menétrey and Willam [16] is adopted and set up in the effective stress space with double hardening and two damage scalars. Appropriate hardening law and damage evolution law are introduced to describe the increase of effective yield stress and the degradation of stiffness. The confining-net decomposition of stress proposed by Zhang et al. [15] is applied to help to account for the suppression of damage evolution in triaxial compression.

1. Framework for Elastoplastic Damage Model. From the confining-net decomposition of stress, a two-scalar damage expression can be formulated as [15]:

$$\sigma = (1 - d^+) \bar{\sigma}^+ + (1 - d^-) \bar{\sigma}^- + \bar{\sigma}^\equiv, \tag{1}$$

where $\bar{\sigma} = \bar{\sigma}^+ + \bar{\sigma}^- + \bar{\sigma}^\equiv$ the components of $\bar{\sigma}$ are defined as

$$\begin{aligned} \bar{\sigma}^+ &= \sum_i \langle \bar{\sigma}_i \rangle_{\rightarrow i} n \otimes n, & \bar{\sigma}^\equiv &= -\langle -\bar{\sigma}_1 \rangle \sum_i n \otimes n, \\ \bar{\sigma}^- &= -\sum_i (\langle -\bar{\sigma}_i \rangle - \langle -\bar{\sigma}_1 \rangle)_{\rightarrow i} n \otimes n, \end{aligned} \tag{2}$$

the Mcauley brackets $\langle \cdot \rangle$ means $\langle x \rangle = \frac{1}{2}(|x| + x)$, d^\pm is the tensile/compressive damage variable, σ is the nominal stress, and $\bar{\sigma}$ is the effective stress. The damage variable for the confining part of stress, d^\equiv , is neglected since there is only residual deformation and hardly stiffness degradation for concrete under hydrostatic compression.

1.1. Damage.

1.1.1. Damage Variables. In this paper, the authors follow a simplified micro-mechanical damage evolution model proposed by Zhang et al. [15] which is an improvement to Li and Ren [17]. The model was extended and could be used in triaxial compression.

Accounting for the definition of stochastic integration, the tensile/compressive damage variable d^\pm can be expressed as

$$d^{\pm} = \int_0^1 H(\varepsilon^{\pm, e} - \Delta^{\pm}(x)) dx, \quad (3)$$

where $H(\cdot)$ is the Heaviside step function, and $\Delta^{\pm}(x)$ is the microscopic random fracture strain.

Because of the presence of the confining part of stress, the damage evolution under uniaxial compression will be suppressed. Zhang et al. [15] take this interaction into account by modifying the microscopic fracture strain:

$$\Delta_{\equiv}^{-}(x) = \Delta^{-}(x) \exp\left(-c_{\Delta} \frac{\langle -\bar{\sigma}_1 \rangle}{f_c}\right), \quad (4)$$

and the compressive damage variable in Eq. (2) becomes

$$d^{-} = \int_0^1 H(\varepsilon^{-, e} - \Delta_{\equiv}^{-}(x)) dx. \quad (5)$$

A more detailed explanation can be found in [15].

1.1.2. *Damage Driving Forces.* Take the tensile/compressive damage energy release rate as the damage driving force:

$$Y^{\pm} = -\frac{\partial \psi}{\partial d^{\pm}}, \quad (6)$$

following the pioneering work by Wu et al. [13], the expressions of Y^{\pm} are given by

$$Y^{+} = \frac{1}{2} \bar{\sigma}^{+} : \varepsilon^e, \quad (7)$$

$$Y^{-} \approx \frac{1}{E} (\alpha \bar{I}_1^{-} + \sqrt{3 \bar{J}_2^{-}})^2, \quad (8)$$

for tension and compression, respectively, where \bar{E} is the effective (initial) Young modulus, \bar{I}_1^{-} is the first invariant of $\bar{\sigma}^{-}$, \bar{J}_2^{-} is the second invariant of the deviatoric part of $\bar{\sigma}^{-}$, and

$$\alpha = \frac{f_{bc}/f_c - 1}{2f_{bc}/f_c - 1}, \quad (9)$$

in which f_c is the uniaxial compressive strength, and f_{bc} is the equi-biaxial compressive strength Y^{+} only involves the elastic free energy ψ^e , while Y^{-} is related to both the elastic ψ^e and plastic ψ^p free energies [18].

1.1.3. *Damage Criteria.* The tensile/compressive damage threshold is defined by the maximum of Y^{\pm} throughout the loading history:

$$r^{\pm} = \max_{\tau \in [0, t]} Y^{\pm}(\tau), \quad (10)$$

where τ is the loading history and t is the current instant.

The tensile/compressive damage criterion is expressed as

$$g^\pm (Y^\pm, r^\pm) = Y^\pm - r^\pm = 0. \quad (11)$$

Damage is driven by the damage thresholds as reflected in a monotonously increasing function:

$$d^\pm = G^\pm (r^\pm). \quad (12)$$

The Karush–Kuhn–Tucker loading/unloading conditions are always expressed as

$$\dot{d}^\pm \geq 0, \quad g^\pm \leq 0, \quad \dot{d}^\pm g^\pm = 0. \quad (13)$$

1.2. **Plasticity.** The plasticity part of the constitutive model is composed of yield criterion, flow rule, hardening laws, evolution of hardening variables and the loading/unloading conditions.

For infinitesimal elastoplastic deformation, the strain tensor ε can be decomposed in an additive sense:

$$\varepsilon = \varepsilon^e + \varepsilon^p. \quad (14)$$

Similarly, for the incremental strain $d\varepsilon$, we have

$$d\varepsilon = d\varepsilon^e + d\varepsilon^p, \quad (15)$$

where ε^e , $d\varepsilon^e$ and ε^p , $d\varepsilon^p$ are the elastic components and plastic components, respectively.

Based on the linear elasticity theory and the hypothesis of elastic strain equivalence, one obtains

$$\sigma = \mathbf{E}:\varepsilon^e, \quad \bar{\sigma} = \bar{\mathbf{E}}:\varepsilon^e, \quad (16)$$

where the rank four tensors \mathbf{E} and $\bar{\mathbf{E}}$, are, respectively, the elastic stiffness for damaged configuration and initial (undamaged) configuration. From Eqs. (14) and (16), the effective stress can be written as

$$\bar{\sigma} = \bar{\mathbf{E}}:(\varepsilon - \varepsilon^p). \quad (17)$$

1.2.1. **Yield Surface.** To apply to various stress states, the yield function proposed by Menétrey and Willam [16] is employed herein. Unlike some other models [1–3] which take the plastic volumetric strain as the variant of hardening/softening function and set up in the nominal stress space, the present paper introduces another approach to express the subsequent yield surface and set it up in the effective stress space. The yield function has the form as

$$f^p(\xi, \rho, \theta) = \left(\sqrt{1.5} \frac{\rho}{f^-} \right)^2 + m \left(\frac{\rho}{\sqrt{6} f^-} r(\theta, e) + \frac{\xi}{\sqrt{3} f^-} \right) - 1 = 0. \quad (18)$$

The three unified cylindrical coordinates ξ , ρ , and θ are defined as the same as previous works except that all of them are expressed as functions of the principal effective stresses ($\bar{\sigma}_1 \geq \bar{\sigma}_2 \geq \bar{\sigma}_3$, compression negative).

The friction parameter m and elliptic function r are given by

$$m = 3 \frac{f^{-2} - f^{+2}}{f^- f^+} \frac{e}{e+1}, \quad (19)$$

$$r(\theta, e) = \frac{4(1-e^2)\cos^2\theta + (2e-1)^2}{2(1-e^2)\cos\theta + (2e-1)[4(1-e^2)\cos^2\theta + 5e^2 - 4e]^{1/2}}, \quad (20)$$

where $f^\pm = f^\pm(k^\pm)$ is the subsequent effective yield stress for uniaxial tension/compression, k^\pm is the internal variable and will be introduced later in Section 1.2.3. The eccentricity parameter e is assumed as 0.52.

From all above, the yield function can be reduced to

$$f^P = f^P(\bar{\sigma}, \mathbf{k}) = 0, \quad (21)$$

where $\bar{\sigma}$ represents the effective stress, and \mathbf{k} represents the vector consisting of two scalars k^\pm .

1.2.2. *Plastic Potential Surface.* A non-associated flow rule and plastic potential function in parabolic type are used here and given by

$$g^P = A \left(\frac{\rho}{f_0^-} \right)^2 + B \frac{\rho}{f_0^-} + \frac{\xi}{f_0^-} \quad (22)$$

in a similar form to that proposed by Carrazedo et al. [2]. How to calibrate the coefficients A and B will be discussed later in Section 3. The plastic strain rate is computed by

$$\dot{\epsilon}^P = \dot{\lambda} \frac{\partial g^P}{\partial \bar{\sigma}}, \quad (23)$$

where $\dot{\lambda}$ is the plastic consistency parameter and is non-negative.

However, it should be noted that the potential plastic function g^P is not only related to the stress $\bar{\sigma}$, but also is related to the internal variables \mathbf{k} . Here, for simplicity, it is assumed that the potential plastic surface does not evolve with the change of the internal variables.

1.2.3. *Hardening Laws.* The hardening law here is formulated by making use of the Ludwik power law:

$$f^\pm(k^\pm) = f_0^\pm + K^\pm (k^\pm)^{n^\pm}, \quad (24)$$

where f_0^\pm is the initial effective yield stress under uniaxial tension/compression, K^\pm is the effective tensile/compressive strength index, k^\pm is the tensile/compressive hardening variable, and n^\pm is the tensile/compressive hardening exponent.

In the present model, the initial effective yield stress can be assumed as $f_0^+ = f_t$, $f_0^- = 0.5f_c$, where f_t and f_c are, respectively, the strengths in uniaxial tension and compression.

The evolution of hardening variables \dot{k}^\pm is given by [15]:

$$\dot{k}^+ = w\dot{\varepsilon}_1^P, \quad \dot{k}^- = -(1-w)\dot{\varepsilon}_3^P \exp\left(-c_k \frac{\langle -\bar{\sigma}_1 \rangle}{f_c}\right), \tag{25}$$

where ε_1^P and ε_3^P are, respectively, the maximum and minimum principal plastic strains, c_k is the coefficient of hardening slowdown, and the weight factor

$$w = \frac{\sum_i \langle \bar{\sigma}_i \rangle}{\sum_i |\bar{\sigma}_i|}. \tag{26}$$

The tensile and compressive hardening functions are

$$h^+ = w \frac{\partial g^P}{\partial \bar{\sigma}_1}, \quad h^- = -(1-w) \frac{\partial g^P}{\partial \bar{\sigma}_3} - \exp\left(-c_k \frac{\langle -\bar{\sigma}_1 \rangle}{f_c}\right). \tag{27}$$

Then the expression of \dot{k}^\pm is rephrased as

$$\dot{k}^\pm = \dot{\lambda} h^\pm. \tag{28}$$

The Karush–Kuhn–Tucker loading/unloading conditions are always expressed as

$$\dot{\lambda} \geq 0, \quad f^P \leq 0, \quad \dot{\lambda} f^P = 0. \tag{29}$$

2. Numerical Implementation. In the numerical implementation process of the proposed model, the plasticity part and damage part are considered separately and a user subroutine is developed. The specific procedure has already been studied maturely and can be summarized in three steps: (i) elastic predictor; (ii) plastic corrector; and (iii) damage corrector. A completely implicit backward-Euler return-mapping algorithm is employed for the constitutive integration. No detailed introduction will be made here. For more information, readers are referred to the literature [19, 20].

3. Calibration. The parameters A and B in the potential plastic function

$$g^P = A \left(\frac{\rho}{f_0^-} \right)^2 + B \frac{\rho}{f_0^-} + \frac{\xi}{f_0^-} \tag{30}$$

must be determined based on the results of uniaxial compression tests and triaxial compression tests with uniform active confinement. Consider the gradient of the potential plastic surface

$$\psi = -\frac{d\xi}{d\rho} = 2A \frac{\rho}{f_0^-} + B. \tag{31}$$

The plastic potential parameters A and B can be derived as

$$A = \frac{1}{2} \frac{\psi_1 - \psi_2}{\rho_1 - \rho_2} f_0^-, \tag{32}$$

$$B = \psi_1 - 2A \frac{\rho_1}{f_0^-}, \quad (33)$$

where the subscript 1 and 2 for ψ and ρ represent the uniaxial compression and triaxial compression with uniform active confinement at peak stress, respectively. The inclination ψ_1 and ψ_2 can be determined by

$$\psi = \frac{\sqrt{2}(\varepsilon_{33}^p - \varepsilon_{11}^p)}{\varepsilon_v^p}. \quad (34)$$

The deviatoric lengths ρ_1 and ρ_2 can be calculated as

$$\rho_1 = \sqrt{\frac{2}{3}} |f_c|, \quad (35)$$

$$\rho_2 = \sqrt{\frac{2}{3}} |f_{cc} - \sigma_{pc}|, \quad (36)$$

where σ_{pc} donates the confining pressure, and f_c and f_{cc} donate the uniaxial and triaxial compression strengths, respectively. The plastic volumetric strain ε_v^p is assumed as

$$\varepsilon_v^p = \frac{f_c}{E_c} (1 - 2\nu) \quad (37)$$

for all stress states. The lateral plastic strains ε_{11}^p and ε_{22}^p are obtained by

$$\varepsilon_{11}^p = \varepsilon_{22}^p = \frac{\varepsilon_v^p - \varepsilon_{33}^p}{2}. \quad (38)$$

Next, we need to determine the values of the axial plastic strain ε_{33}^p , lateral stresses σ_{11} and σ_{22} , and axial stress σ_{33} . For uniaxial compression

$$\varepsilon_{33}^p = \varepsilon_{33} - \frac{1}{E_c} [f_c - \nu(0+0)] = \varepsilon_c - \frac{f_c}{E_c}. \quad (39)$$

The calculation of ε_c follows the recommendations of MC90 [21] and CEB Working Group on HSC/HPC [22]:

$$\varepsilon_c = -\min \begin{cases} 0.0022, \\ 0.7 f_c^{0.31} \\ 1000 \end{cases}. \quad (40)$$

For triaxial compression with uniform active confinement:

$$\varepsilon_{33}^p = \varepsilon_{33} - \frac{1}{E_c} [\sigma_{33} - \nu(\sigma_{11} + \sigma_{22})] = \varepsilon_{cc} - \frac{1}{E_c} [f_{cc} - 2\nu\sigma_{pc}]. \quad (41)$$

The ultimate axial stress f_{cc} is estimated from the expression by Carrazedo et al. [2]:

$$f_{cc} = \frac{f_c}{2} \left(\frac{2\sigma_{pc}}{f_c} + \sqrt{\frac{40.642\sigma_{pc}}{f_c} + 4} \right). \quad (42)$$

The total axial strain at triaxial stress is obtained from the expression by Papanikolaou and Kappos [4]:

$$\varepsilon_{cc} = \varepsilon_c \left(1 + 17 \frac{\sigma_{pc}}{f_c} \right), \quad (43)$$

where σ_{pc} represents the confining pressure.

4. Verification. To examine the rationality and practicability of the present constitutive model, numerical simulations of a series of standard concrete tests were carried out and compared with the existing experimental results. The simulations of uniaxial loading tests, including monotonous loading, and cyclic loading, are the same as the results in Zhang et al. [15] and will not be discussed here again.

4.1. Tension–Compression Reversed Loading. In this section, two tension–compression reversed loading scenarios were simulated, while one is compression-dominated, the other is tension-dominated. No comparative experimental data were found. The material parameters are calibrated from the cyclic uniaxial compression test [23]. The stress–strain responses for such loadings are given in Fig. 1. The unilateral effect and the crack-opening, crack-closing are exhibited.

4.2. Biaxial Compression. The experiments by Kupfer et al. [24] are chosen for the simulations of biaxial compression loading, as shown in Fig. 2.

4.3. Pseudo Triaxial Compression. A triaxial compression test with uniform confinement ($0 > \sigma_1 = \sigma_2 > \sigma_3$) is simulated. The purpose is to study whether the present model can reflect the enhancement of strength and improvement of ductility under confinement. Four different confining pressures were considered, i.e., $\sigma_1 = \sigma_2 = -4$ MPa, $\sigma_1 = \sigma_2 = -8$ MPa, $\sigma_1 = \sigma_2 = -12$ MPa, and $\sigma_1 = \sigma_2 = -4$ MPa. In these tests, after the hydrostatic pressure was increased to the desired value, the axial displacement loading started. The material parameters are calibrated from the experimental uniaxial stress–strain curves and stress–strain curves under the confining pressure $\sigma_1 = \sigma_2 = -4$ MPa, then the same set of material parameters are used to predict the behavior under $\sigma_1 = \sigma_2 = -8$ MPa and $\sigma_1 = \sigma_2 = -12$ MPa. The material parameters are listed in Table 1. The calculation results and comparison with Candappa et al. [25] were shown in Fig. 3.

Table 1

Material Parameters for Simulations of Uniaxial Reversed Loading

\bar{E} , N/mm ²	ν	μ^+	μ^-	V^+	V^-
$50.9 \cdot 10^3$	0.2	–	7.75	–	0.75
f_0^+	f_0^-	K^+	K^-	n^+	n^-
–	16.7	–	$0.035\bar{E}$	–	0.5
c_Δ	c_k	f_t	f_c	A	B
–	–	–	60.6	1.57	0.65

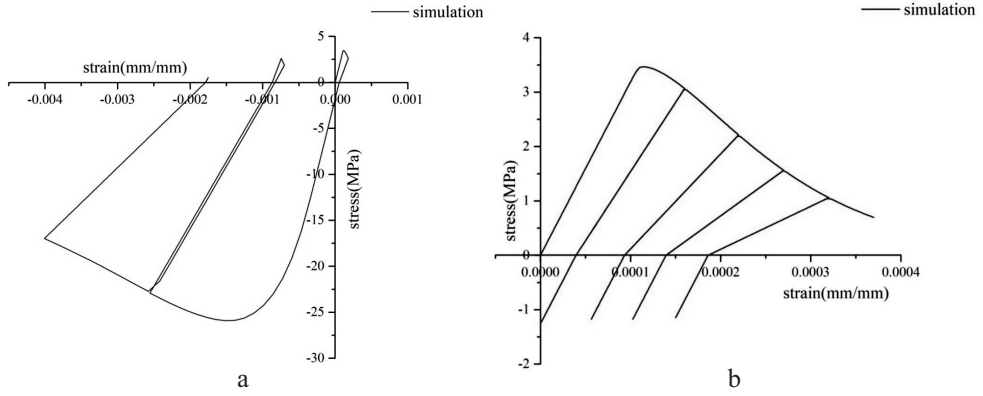


Fig. 1. Compression- (a) and tension-dominated (b) reversed loadings.

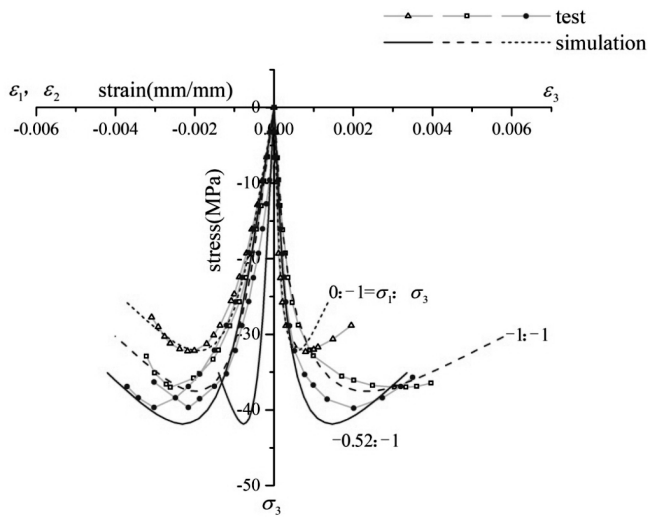


Fig. 2. Biaxial compression [24].

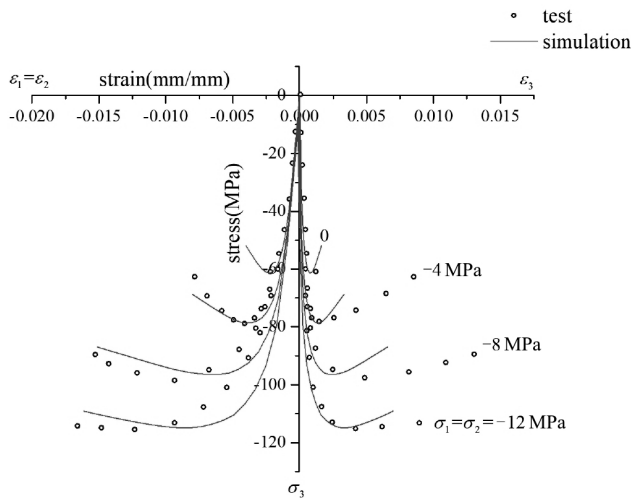


Fig. 3. Pseudo triaxial compression [25].

Although there is a small amount of deviation between simulation and experiment, the increase of peak strength and the improvement of ductility under confinement have been appropriately represented in the proposed model.

4.4. True Triaxial Compression. In fact, pseudo triaxial compression is an ideal stress state. In practical cases, concrete is usually in a complex stress state. Here, the authors have examined the model in true triaxial states. Simulations of true triaxial compression ($0 > \sigma_1 > \sigma_2 > \sigma_3$) are attempted based on the tests by van Mier [26] and displayed in Fig. 4. The test data from the loading path $\sigma_1:\sigma_2:\sigma_3 = -0.05:-0.1:-1$ are used for parameter calibration, and those from $\sigma_1:\sigma_2:\sigma_3 = -0.05:-0.33:-1$ are blindly predicted.

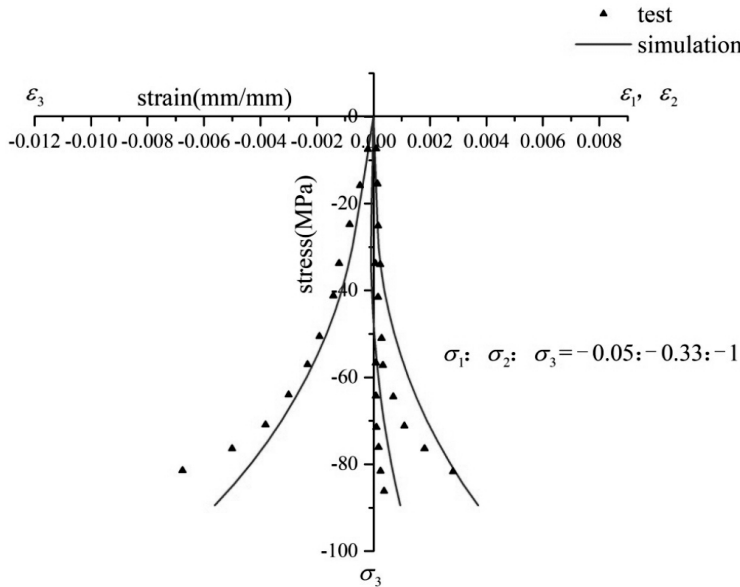


Fig. 4. True triaxial compression [26].

Conclusions. By the combination of the confining-net decomposition of stress with the Menétrey–Willam yield function and the Ludwik power hardening law, the constitutive model proposed in this study achieves a more accurate description of the mechanical behavior of concrete in triaxial compression. With the aid of the positive-negative decomposition of stress, double hardening, and two-parameter damage, the model also performs satisfactorily in reversed tension and compression. Several numerical examples have preliminarily demonstrated the capabilities of this versatile 3D elastoplastic damage model. Further study is underway to extend the present theory to very high confining pressure and large deformation.

Acknowledgments. Financial support by the National Science Foundation of China (NSFC) (Grant No. 51378377) and Fundamental Research Funds for the Central Universities (Grant No. 2016YXMS094) is much appreciated.

1. J. Q. Bao, X. Long, K. H. Tan, and C. K. Lee, “A new generalized Drucker–Prager flow rule for concrete under compression,” *Eng. Struct.*, **56**, 2076–2082 (2013).
2. R. Carrazedo, A. Mirmiran, and J. B. de Hanai, “Plasticity based stress-strain model for concrete confinement,” *Eng. Struct.*, **48**, No. 48, 645–657 (2013).
3. P. Grassl, K. Lundgren, and K. Gylltoft, “Concrete in compression: a plasticity theory with a novel hardening law,” *Int. J. Solids Struct.*, **39**, No. 20, 5205–5223 (2002).

4. V. K. Papanikolaou, and A. J. Kappos, "Confinement-sensitive plasticity constitutive model for concrete in triaxial compression," *Int. J. Solids Struct.*, **44**, No. 21, 7021–7048 (2007).
5. R. K. Abu Al-Rub and S. M. Kim, "Computational applications of a coupled plasticity-damage constitutive model for simulating plain concrete fracture," *Eng. Fract. Mech.*, **77**, No. 10, 1577–1603 (2010).
6. J. Červenka and V. K. Papanikolaou, "Three dimensional combined fracture-plastic material model for concrete," *Int. J. Plasticity*, **24**, No. 12, 2192–2220 (2008).
7. U. Cicekli, G. Z. Voyiadjis, and R. K. Abu Al-Rub, "A plasticity and anisotropic damage model for plain concrete," *Int. J. Plasticity*, **23**, Nos. 10–11, 1874–1900 (2007).
8. P. Grassl and M. Jirásek, "Damage-plastic model for concrete failure," *Int. J. Solids Struct.*, **43**, Nos. 22–23, 7166–7196 (2006).
9. L. Jason, A. Huerta, G. Pijaudier-Cabot, and S. Ghavamian, "An elastic plastic damage formulation for concrete: Application to elementary tests and comparison with an isotropic damage model," *Comput. Method. Appl. M.*, **195**, No. 52, 7077–7092 (2006).
10. O. Omidi and V. Lotfi, "Finite element analysis of concrete structures using plastic-damage model in 3-D implementation," *Int. J. Civil Eng.*, **8**, No. 3, 187–203 (2010).
11. P. J. Sánchez, A. E. Huespe, J. Oliver, et al., "A macroscopic damage-plastic constitutive law for modeling quasi-brittle fracture and ductile behavior of concrete," *Int. J. Numer. Anal. Met.*, **36**, No. 5, 546–573 (2012).
12. G. Z. Voyiadjis, Z. N. Taqieddin, and P. I. Kattan, "Anisotropic damage–plasticity model for concrete," *Int. J. Plasticity*, **24**, No. 10, 1946–1965 (2008).
13. J. Y. Wu, J. Li, and R. Faria, "An energy release rate-based plastic-damage model for concrete," *Int. J. Solids Struct.*, **43**, Nos. 3–4, 583–612 (2006).
14. J. Zhang and J. Li, "Elastoplastic damage model for concrete based on consistent free energy potential," *Sci. China Tech. Sci.*, **57**, No. 11, 2278–2286 (2014).
15. J. Zhang, J. Li, and J. W. Ju, "3D elastoplastic damage model for concrete based on novel decomposition of stress," *Int. J. Solids Struct.*, **94–95**, 125–137 (2016).
16. P. Menetrey and K. J. Willam, "Triaxial failure criterion for concrete and its generalization," *ACI Struct. J.*, **92**, No. 3, 311–318 (1995).
17. J. Li and X. D. Ren, "Stochastic damage model for concrete based on energy equivalent strain," *Int. J. Solids Struct.*, **46**, No. 11, 2407–2419 (2009).
18. J. Zhang and J. Li, "Microelement formulation of free energy for quasi-brittle materials," *J. Eng. Mech.*, **140**, No. 8, 06014008 (2014).
19. J. W. Ju, "On energy-based coupled elastoplastic damage theories: Constitutive modeling and computational aspects," *Int. J. Solids Struct.*, **25**, No. 7, 803–833 (1989).
20. J. Zhang and J. Li, "Semi-implicit algorithm for elastoplastic damage models involving energy integration," *Adv. Mater. Sci. Eng.*, **2016**, Article ID 5289642 (2016), DOI: 10.1155/2016/5289642.
21. *CEB-FIP Model Code 90*, No. 213/214, Bulletin d'Information CEB, Lausanne (1993).
22. *High Performance Concrete: Recommended Extensions to the Model Code 90*, Research Needs, CEB-FIP Working Group on High Strength/High Performance Concrete, CEB (1995).

23. A. I. Karsan and J. O. Jirsa, "Behavior of concrete under compressive loadings," *J. Struct. Div.-ASCE*, **95**, 2535–2563 (1969).
24. H. B. Kupfer, H. K. Hilsdorf, and H. Rusch, "Behavior of concrete under biaxial stresses," *ACI Struct. J.*, **66**, No. 8, 656–666 (1969).
25. D. C. Candappa, J. G. Sanjayan, and S. Setunge, "Complete triaxial stress–strain curves of high-strength concrete," *J. Mater. Civil Eng.*, **13**, No. 3, 209–215 (2001).
26. J. G. M. van Mier, *Strain-Softening of Concrete under Multiaxial Loading Conditions*, Technische Hogeschool Eindhoven, Eindhoven (1984), DOI: 10.6100/IR145193.

Received 05. 03. 2018